Eur. J. Mech. B - Fluids 20 (2001) 233–254

S0997-7546(00)01117-1/FLA

Large-eddy simulation of a turbulent forced plume

Xu Zhou *, Kai H. Luo, John J.R. Williams

Department of Engineering, Queen Mary and Westfield College, University of London, Mile End Road, London E1 4NS, UK

(Received 15 July 1999; revised 15 March 2000 and 22 June 2000; accepted 13 October 2000)

Abstract – This paper reports on an application of large-eddy simulation (LES) to a spatially-developing round turbulent buoyant jet. The numerical method used is based on a low-Mach-number version of the governing equations for compressible flow which can account for density variations. The second-order centre-difference scheme is used for spatial discretization and an Adams–Bashforth scheme for temporal discretization. Comparisons are made between LES results, experimental measurements and plume theory for the forced plume under moderate Reynolds number and good agreement has been achieved. It is found that the plume spreading and the centerline maximum mean velocity strongly depend on the forcing conditions imposed on the inflow plane. The helical mode of instability leads to a larger spreading rate as compared to an axisymmetric mode. The enhanced entrainment is directly related to the strong turbulent momentum and energy transports between the plume and surrounding fluid induced by vortex dynamics. The entrainment ratio is about 0.09 and falls into the range of experimentally determined values. Budgets of the mean momentum and energy equations are analyzed. It is found that the radial turbulent transport nearly balances the streamwise convection and the buoyancy force in the axial momentum equation. Also, the radial turbulent stress is balanced by the streamwise convection in the energy equation. The energy-spectrum for the axial velocity fluctuations shows a $-5/3$ power law of the Kolmogorov decay, while the power spectrum for the temperature fluctuations shows both $-5/3$ and -3 power laws in the inertial-convective and inertial-diffusive ranges, respectively. © 2001 Éditions scientifiques et médicales Elsevier SAS

LES / buoyancy / turbulent plume

1. Introduction

Buoyant jets and plumes are of great interest due to their effect on mixing and entrainment. Plumes "arise when buoyancy is supplied steadily and the buoyant region is continuous between the source and the level of interest" (Turner [1]). The main difference between a jet and plume is that a jet is momentum-driven whilst a plume is buoyancy-dominated. A so-called forced plume is a kind of flow between a pure jet and a pure plume and it is driven by both buoyancy and momentum by discharging light fluid into the atmosphere. Hereafter, when we refer to a plume we in fact mean a forced turbulent plume and this is the subject of this paper. In most plume experiments without chemical reaction, fluid either of high temperature or of low density is injected into the ambient air. Both of these can result in density inhomogeneity which can produce different phenomena from that of constant-density jets. Forced jets and plumes are common in many aspects such as: transition from laminar to turbulent state in the near-field, self-similarity in the far-field, air entrainment identified by the engulfing of ambient fluid by the large eddies and jet spreading, etc. The basic spatial and temporal features of the plume are controlled by dynamics similar to cold jets. The large amount of existing work for pure jets (Urbin and Metais [2]; Crow and Champagne [3]; Yuan et al. [4]) can therefore be of great benefit to the understanding of plumes.

* Correspondence and reprints. Present address: Department of Mechanical and Aerospace Engineering, Rutgers University – The State University of New Jersey, 98 Brett Road, Piscataway, NJ 08854-8058, USA.

E-mail addresses: X.Zhou@qmw.ac.uk (X. Zhou), K.H.Luo@qmw.ac.uk (K.H. Luo), J.J.R.Williams@qmw.ac.uk (J.J.R. Williams).

Large-eddy simulation (LES) has been applied to many fluid flows but most of these have been limited to those with uniform-density. Very little work has, however, been carried out for thermal buoyant jets. To the author's knowledge, large eddy simulations of spatially evolving free plumes are still rare especially when compared with available experimental data and plume theory. Nam and Bill [5] used a modified $k-\varepsilon$ turbulence model to simulate thermal plumes and obtained good agreement with experimental data. However, this kind of traditional method cannot give a clear picture of detailed fluctuating flow. LES has the advantage that its solution is less model-dependent and that it can show instantaneous large-scale structures as well as providing statistics. In LES, the large eddies are resolved numerically while the fine-scale eddies are modeled by a subgrid scale (SGS) model. The feature of capturing large-scale motions in LES is of great value to practical applications such as thermal plumes. Although direct numerical simulation (DNS) has the advantage of being more accurate than LES, LES is, unlike DNS, not restricted to low Reynolds numbers.

One of the more practical uses of LES is to predict the transition and subsequent turbulent mixing (or spreading) process that occurs in spatially developing flows. As is well known, a free jet is subject to Kelvin–Helmholtz instability which, in turn, means that the flow is unstable to small exponentially growing disturbances and many linear instability analyses have confirmed this growth (Michalke [6]; Luo and Sandham [7]). The thin shear layer in a free jet with an initially top-hat profile undergoes several stages of development: Kelvin–Helmholtz instability followed by the rolling up of vortices, pairing and merging processes and the breakdown of the potential core with the advent of spreading by the secondary three-dimensional instability mechanism. Grinstein and DeVore [8] showed a transition to turbulence in free square jets characterized by the dynamics of vortex rings and braid vortices and observed a larger entrainment rate to those found in round jets. Zaman [9] analyzed the influence of jet geometry on the characteristics of spreading from subsonic to supersonic flow. They observed a substantial increase of jet spreading when tabs were inserted at the nozzle which induced streamwise vortex pairs. Vortex dynamics are also expected to be important in the control of plume instability, transition from the momentum to buoyancy dominated region and even the plume development further downstream. It should be noted that vortex stretching (which cannot be captured by a two-dimensional numerical simulation of a jet) is vital in maintaining high levels of fluctuating vorticity, a major characteristic of rotational three-dimensional turbulent flows (Tennekes and Lumley [10]).

According to the experiments by George et al. [11] and Shabbir and George [12], the plume achieves its turbulent state within two diameters. Other investigators, however, in conducting LES or DNS of jets (Urbin and Metais [2]; Boersma et al. [13]), have shown that the length of the potential core lies between 5–8 jet diameters if white noise is imposed on the jets. There are several ways to achieve an earlier spatial development of turbulence. A survey of free jets shows that the evolution of an azimuthal instability mode can lead to an earlier breakdown and transition from laminar to turbulence. Menon and Rizk [14] unlike others, used a parabolic profile to trigger a jet preferred mode of instability and bypass the natural shear layer instability to obtain an earlier breakdown. Higher forcing of perturbations can also reduce the length of the laminar zone. We, therefore, adopted a higher level of forcing in combination with an azimuthal mode of instability at the inlet in order to get consistent results with experiment ([11,12]).

Plume theory (Turner [1]) which was developed from experimental and theoretical work, has existed for several decades but has been recently modified by many researchers (Rooney and Linden [15]; Woods [16]). The basic ideas involved in plume theory are: the Boussinesq approximation, the similarity and entrainment assumptions. The entrainment assumption, which is less often used as compared to the other two assumptions, is to obtain the entrainment ratio by integrating the simplified Navier–Stokes governing equations (mass, momentum and energy) in terms of top-hat variables. The similarity assumption assumes that a plume spreads linearly with height and that the mean flux across the edge of the plume (E) is proportional to the local vertical velocity (W). More recently, Rooney and Linden [15] and Woods [16] modified the similarity form

for non-Boussinesq plumes. It was found from plume theory and experimental data that the parameter which characterized these flows was the entrainment ratio having a value of about 0.1.

Most of the experimental and theoretical work on plumes has been concentrated on the far-field self-similar region (Dai et al. [17]; List [18]). Dai et al. [17] carried out an experimental study of fully developed turbulent plumes extending far from the source (e.g. up to 150 source diameters). According to their observation, the self-similar region can only be achieved after about 80 diameters. They found that the temporal spectra exhibit the well-known $-5/3$ and $-3/1$ power laws in agreement with the findings by Noto et al. [19] and Papanicolaou and List [20]. George et al. [11] and Shabbir and George [12], on the other hand, presented detailed experimental statistics up to third-order for round buoyant plumes with hot air as the fluid medium. Their measured positions lay in the range of 8–25 diameters from the inlet and provide good data to compare with our LES results obtained with a computational domain that does not require excessively high CPU hours.

The objective of this paper is to simulate a turbulent plume using LES aimed at obtaining a more complete picture and clearer physical understanding of the plume from the near-field laminar region to the far-field turbulent mixing region; something that has not been addressed in most plume experiments and the plume theory. This paper is divided into three parts. In the first part, the governing equations for 3D low-Mach-number variable-density flows are discussed briefly together with a subgrid scale model for LES. Secondly, the numerical scheme and solution procedure are given. In the last part we investigate the numerical results of the forced plume together with detailed discussions. The plume dynamics are analyzed from different aspects, e.g. transition processes, self-similarity and budgets. Numerical results are compared with the available experimental work of George et al. [11], Shabbir and George [12] and the plume theory mentioned above.

2. Governing equations and closure model

The present paper adopts a projection method for low-Mach-number weakly compressible flows. The variable-density characteristics can be accounted for in the present LES of buoyant jets without a Boussinesq approximation. The 3D filtered continuity, momentum and energy conservation equations in Cartesian coordinates are as follows:

$$\frac{\partial \overline{\rho}}{\partial t} + \frac{\partial}{\partial x_j}(\overline{\rho}\tilde{u}_j) = 0, \tag{1}$$

$$\frac{\partial(\overline{\rho}\tilde{u}_i)}{\partial t} + \frac{\partial(\overline{\rho}\tilde{u}_i\tilde{u}_j)}{\partial x_j} = -\frac{\partial \overline{p^{(1)}}}{\partial x_i} + \frac{\partial \overline{S}_{ij}}{\partial x_j} + (\rho_a - \overline{\rho})g_i - \frac{\partial \tau_{ij}}{\partial x_j} \quad (i = 1, 2, 3), \tag{2}$$

$$\frac{\partial(\overline{\rho}\tilde{h})}{\partial t} + \frac{\partial(\overline{\rho}\tilde{u}_j\tilde{h})}{\partial x_j} = \frac{\partial}{\partial x_j}\left[\left(\frac{\lambda}{c_p}\right)\cdot\frac{\partial \tilde{h}}{\partial x_j}\right] - \frac{\partial Q_j}{\partial x_j}, \tag{3}$$

where the Einstein convention of summation over repeated indices is adopted. μ, λ, c_p are the molecular viscosity, thermal conductivity and specific heat. $\tilde{u}_i = \overline{\rho u}_i/\overline{\rho}$ and $\tilde{h} = \overline{\rho h}/\overline{\rho}$ are Favre-filtered velocity and enthalpy, ρ_a is the density of ambient air and $p^{(1)}$ is the hydrodynamic pressure. The density comes from the state equation of ideal gas, $p^{(0)} = \overline{\rho} R \overline{T}$, where the zeroth-order thermodynamic pressure, $p^{(0)}$, is used and is equal to the atmospheric pressure. The gravitational force term, g_i, is included to account for the buoyancy effect and is usually added along the negative vertical direction. $\tau_{ij} = \overline{\rho u_i u_j} - \overline{\rho}\tilde{u}_i\tilde{u}_j$ is the subgrid scale Reynolds stress, $Q_j = \overline{\rho u_j h} - \overline{\rho}\tilde{u}_j\tilde{h}$ the subgrid scale heat flux and $\overline{S}_{ij} = -\frac{2}{3}\mu\frac{\partial \tilde{u}_k}{\partial x_k}\delta_{ij} + \mu(\frac{\partial \tilde{u}_i}{\partial x_j} + \frac{\partial \tilde{u}_j}{\partial x_i})$ the molecular strain rate tensor. The unknown SGS correlation τ_{ij} and Q_{ij} require closure models. The present large-eddy simulation implicitly applies a box filter in each direction.

The subgrid terms representing the cascade of energy from the large to the small scales are modeled based on the assumption that the small scales are universal and contain only a small amount of energy. The non-resolvable small scale turbulence can be represented by a subgrid model, e.g. Smagorinsky, similarity, gradient and dynamic models. The standard Smagorinsky SGS model is still the most widely used and is adopted here. The modeled subgrid stress tensor τ_{ij} takes the form as follows based on the eddy-viscosity approach:

$$\tau_{ij} = \overline{\rho}(\widetilde{u_i u_j} - \tilde{u}_i \tilde{u}_j) = -\mu_e \tilde{S}_{ij}, \tag{4}$$

where μ_e is the eddy viscosity, $\mu_e = \overline{\rho} l^2 \Pi_{\tilde{S}}^{1/2}$, where $\Pi_{\tilde{S}} = \frac{1}{2}\tilde{S}_{ij}\tilde{S}_{ij}$, $\tilde{S}_{ij} = (\frac{\partial \tilde{u}_i}{\partial x_j} + \frac{\partial \tilde{u}_j}{\partial x_i}) - \frac{2}{3}\frac{\partial \tilde{u}_k}{\partial x_k}\delta_{ij}$. The subgrid length l is assumed to be proportional to the filter width Δ which is then related to the grid spacings in three dimensions:

$$l = C_s \Delta = C_s (\Delta x \Delta y \Delta z)^{1/3}. \tag{5}$$

The subgrid scale model for the turbulent thermal energy flux Q_j is as follows,

$$Q_j = \overline{\rho}(\widetilde{u_j h} - \tilde{u}_j \tilde{h}) = -\frac{\mu_e}{Pr_e}\frac{\partial \tilde{h}}{\partial x_j}. \tag{6}$$

The most commonly used standard Smagorinsky constant $C_s = 0.1$ and the turbulent Prandtl number $Pr_e = 0.3$ are applied here.

3. Numerical scheme

Variables are discretized using a staggered grid with uniform cell size in a 3D rectangular domain. Velocity components are specified at cell faces, while the scalar variables such as enthalpy, temperature and density are located at cell centers. A second-order Adams–Bashforth time integration scheme is used to advance the velocity and scalar fields and a second-order central difference scheme is used for the space discretization in Cartesian coordinates. A projection method (Najm et al. [21]) is used to couple the momentum and continuity equations and the resulting Poisson equation is solved by a multi-grid method.

The discrete scheme for the convective terms needs some special treatment for the energy equation. For example, the convective term in a cell center along x-direction is expressed as the quantities at cell faces 'w' and 'e' (the overline and tilde are ignored)

$$\left.\frac{\partial(\rho u h)}{\partial x}\right|_c = \frac{1}{2}\left[(\rho u)_e \left.\frac{\partial h}{\partial x}\right|_e + (\rho u)_w \left.\frac{\partial h}{\partial x}\right|_w\right], \tag{7}$$

instead of

$$\left.\frac{\partial(\rho u h)}{\partial x}\right|_c = \frac{(\rho u h)_e - (\rho u h)_w}{\Delta x}. \tag{8}$$

The former gives a more stable solution, because the continuity equation is implicitly applied.

The governing equations (1)–(3) must be supplemented by initial and boundary conditions. At the inflow all variables are known including velocities (or mass fluxes) and temperature (or enthalpy). The vertical velocity, u, is specified as a function of radial position while the other two velocity components, v, w, are small random numbers. Although the use of rectangular grid for the circular jet may cause some stepped edges around the jet boundary, especially close to the plume source, the effect is considered to be negligible. Note that this kind of treatment has also been successfully used in other LES applications (Urbin and Metais [2]; Olsson and Fuchs

[22]). At the lateral boundary, a pressure boundary condition is used, whereby the pressure is kept constant and the mass fluxes are calculated through the continuity equation. Thus ambient fluid can enter into the plume through the normal direction. This kind of boundary condition works quite well as the 'traction-free' boundary condition used by Boersma et al. [13]. If a free-slip boundary condition is applied, no entrainment is possible and the structures of the streamlines are greatly changed (see Fig. 3(a) of Boersma et al. [13]). A free buoyant jet is numerically unstable at the outflow boundary. In a compressible flow, one can use arguments about characteristics and the direction of propagation of information to design non-reflecting boundary conditions. However, in an incompressible or low-Mach-number flow this is not possible. A higher co-flow velocity can be employed to ensure stability, but it is found that the length of potential core and the spreading rate are strongly affected by the co-flow velocity in a plume. For the present study, a zero-velocity-gradient condition is applied at the outflow boundary and, in addition, we keep the velocity positive at the outlet to ensure a stable solution as reverse flow can cause numerical instability. This kind of boundary condition has only a small influence on the domain next to the outflow boundary.

4. Results and discussion

A simulation has been carried out of a vertical round jet with heated air as the injection fluid. The jet axis is aligned with the gravity vector and is subjected to a positive buoyancy force. The heat source diameter D is 6.35 cm, the exit mean velocity U_0 is 0.98 m/s, the inflow temperature T_0 is 568 K and the ambient air temperature T_a is 300 K. The corresponding Reynolds number is 1273, based on the inflow mean velocity, viscosity and diameter. The inflow conditions are taken to be the same as in the experiment of Shabbir and George [12]. Unless indicated otherwise, the experimental data to be compared with refer to that obtained by George et al. [11]. The computational grid is composed of $256 \times 128 \times 128$ cells in a box of size $16 \times 8 \times 8$ diameters (grid I). Another domain of box of size $8 \times 4 \times 4$ diameters (grid II) with the same grids as above was used to check the effect of numerical resolution on the plume dynamics. The coarse grid (I) is mainly used to get statistical results extending to a relatively fully-developed region. The time step was set to 0.00025 (s) at grid I in order to keep the Courant number less than 0.2. The numerical method outlined above was implemented on a Cray-T3E massively parallel computer using 64 processors. The computational domain was divided into 64 blocks with each one running on an individual processor. The total computation time normalized by D/U_0 was about 100 and, typically, about 4000 PE hours were required for each simulation.

The source buoyancy and specific momentum per second are defined as

$$F_0 = 2\pi g \int_0^\infty \left(U \frac{\Delta T}{T} + \frac{\overline{u'T'}}{T} \right) r \, \mathrm{d}r, \qquad M_0 = 2\pi \int_0^\infty U^2 r \, \mathrm{d}r, \tag{9}$$

where r is the radius.

The Morten length scale is defined as:

$$L_M = M_0^{3/4} / F_0^{1/2}, \tag{10}$$

which is a characteristic length scale measuring the degree of jet-like or plume-like behavior. The flow parameters at the plume source are listed in *table I*.

Table I. Flow parameters at the inlet.

D (m)	T_a (K)	T_0 (K)	U_0 (m/s)	F_0 (m^4/s^3)	M_0 (m^4/s^2)	$Re = \frac{\rho U_0 D}{\mu}$	$Fr = \frac{U_0^2}{gD}$
0.0635	300	568	0.98	0.0127	0.003	1273	1.54

4.1. Transition to turbulence

A top-hat velocity profile was used at the inflow plane and is given as follows (Michalke [6]):

$$U_0(r) = 0.5U_0\big[1 - \tanh\big[b_2\big(2r/D - D/(2r)\big)\big]\big], \tag{11}$$

where $b_2 = 0.25R_{\frac{1}{2}}/\theta$ and $R_{\frac{1}{2}}/\theta$ is set to 25.

A free plume can undergo transition from laminar to turbulence with an abrupt breakdown of the potential core due to the growth of disturbances. As is well known, the length of the potential core strongly depends on the disturbances added at the inlet. In this study, an azimuthal disturbance combined with a high level of forcing is employed in order to get consistent results to that of Shabbir and George [12] who showed that the plume became turbulent at a very short distance from the exit.

To excite the flow the fluctuating axial velocity at the inflow plane takes the following form (Menon and Rizk [14])

$$u' = AU_0(r)\sum_{n=1}^{N}\sin(2\pi f t/n + \theta), \tag{12}$$

where A is the amplitude of forcing and N is the number of modes (set to 6). Therefore the fluctuating axial velocity is specified as a function of time, t, and polar azimuthal angle, θ. The frequency f is determined by the jet preferred mode corresponding to a Strouhal number of 0.3. With $\theta = 0$ axisymmetric forcing is imposed, otherwise it is of azimuthal forcing. Here a relatively high level of disturbance is imposed with an amplitude of 20% of the mean velocity. The other two velocity components are forced with a smaller amplitude of the mean axial velocity ($0.01U_0$). It should be noted that although a relatively high level of forcing is applied, the transition from laminar to turbulent flow cannot be bypassed totally by the present LES (as will become evident from the following results).

Figure 1(a) shows the energy-spectrum for the buoyant jet based on the temporal axial velocity fluctuations (taken over 20 forcing periods) at $x/D = 4$ along the centerline. It can be seen that the inertial range obeys the $-5/3$ Kolmogorov power law. In *figure 1(b)* the spectrum for the temperature fluctuations initially shows a similar trend in the so-called inertial-convective region and this is then followed by a region where the spectrum

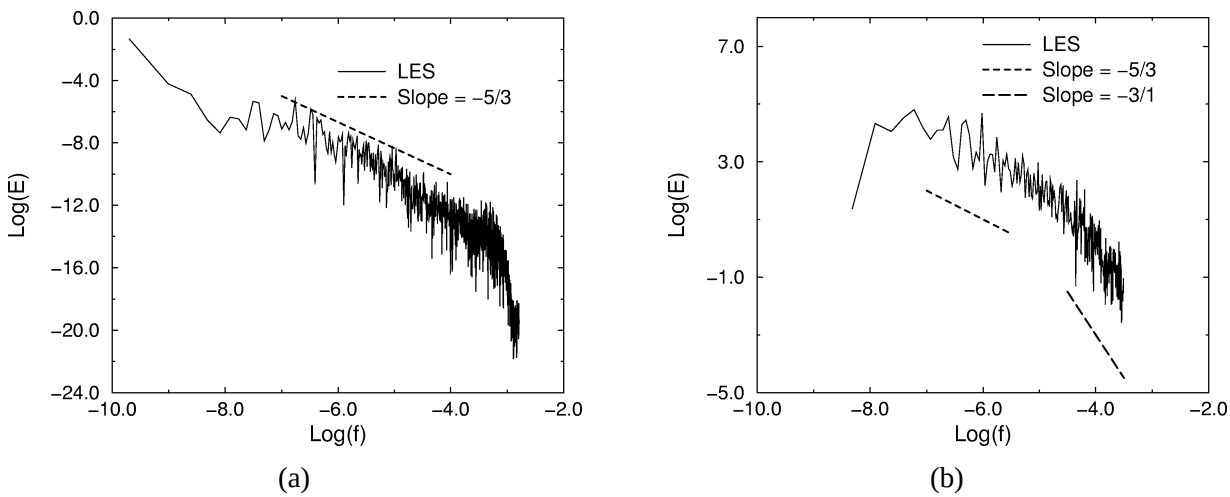

Figure 1. Temporal power spectrum based on: (a) the centerline velocity, and (b) the centerline temperature at $x/D = 4$.

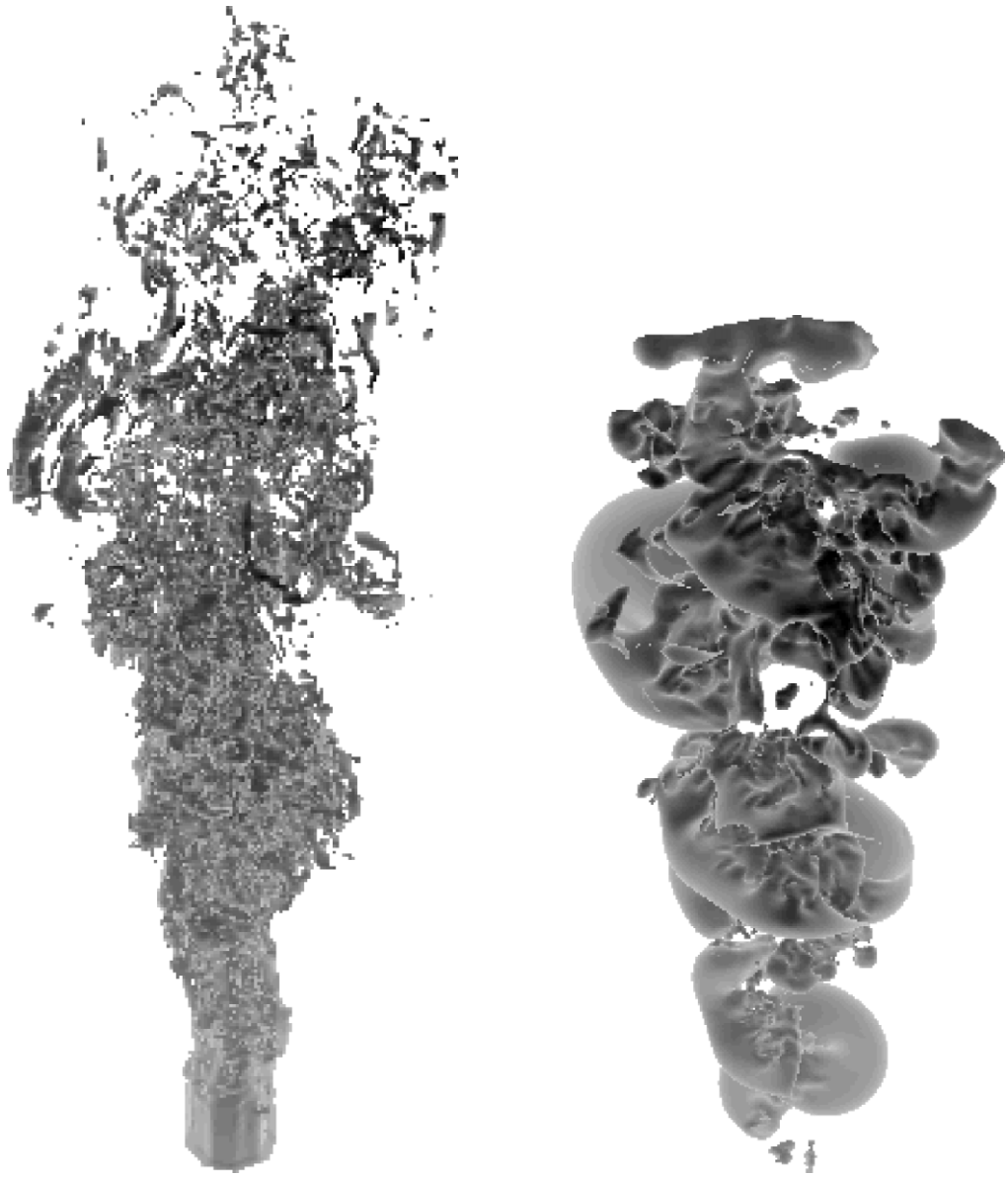

Figure 2. Instantaneous three-dimensional snapshot of (a) vorticity magnitude ($\omega = 0.6$), and (b) hydrodynamic pressure ($p = 0.024$), in the plume with azimuthal forcing with grid I.

decays more rapidly with a -3 power decay law. This is a special feature of buoyant jet flows and expected for the inertial-diffusive subrange suggested by List [18] and Kotsovinos [23]. It is evident, therefore, that buoyancy has a strong effect on the turbulence spectrum. It has also been experimentally observed by Dai et al. [17] and Noto et al. [19] in highly buoyant flows. Kotsovinos [23] argued that the 'jump' from $-5/3$ to -3 subrange was a result of stronger energy feeding due to large plume vortices driven by buoyancy force.

As indicated by Yuan et al. [4], examination of vorticity and pressure can provide a more complete picture of large-scale structures of the flow field. *Figure 2(a)* shows an instantaneous three-dimensional iso-surface with

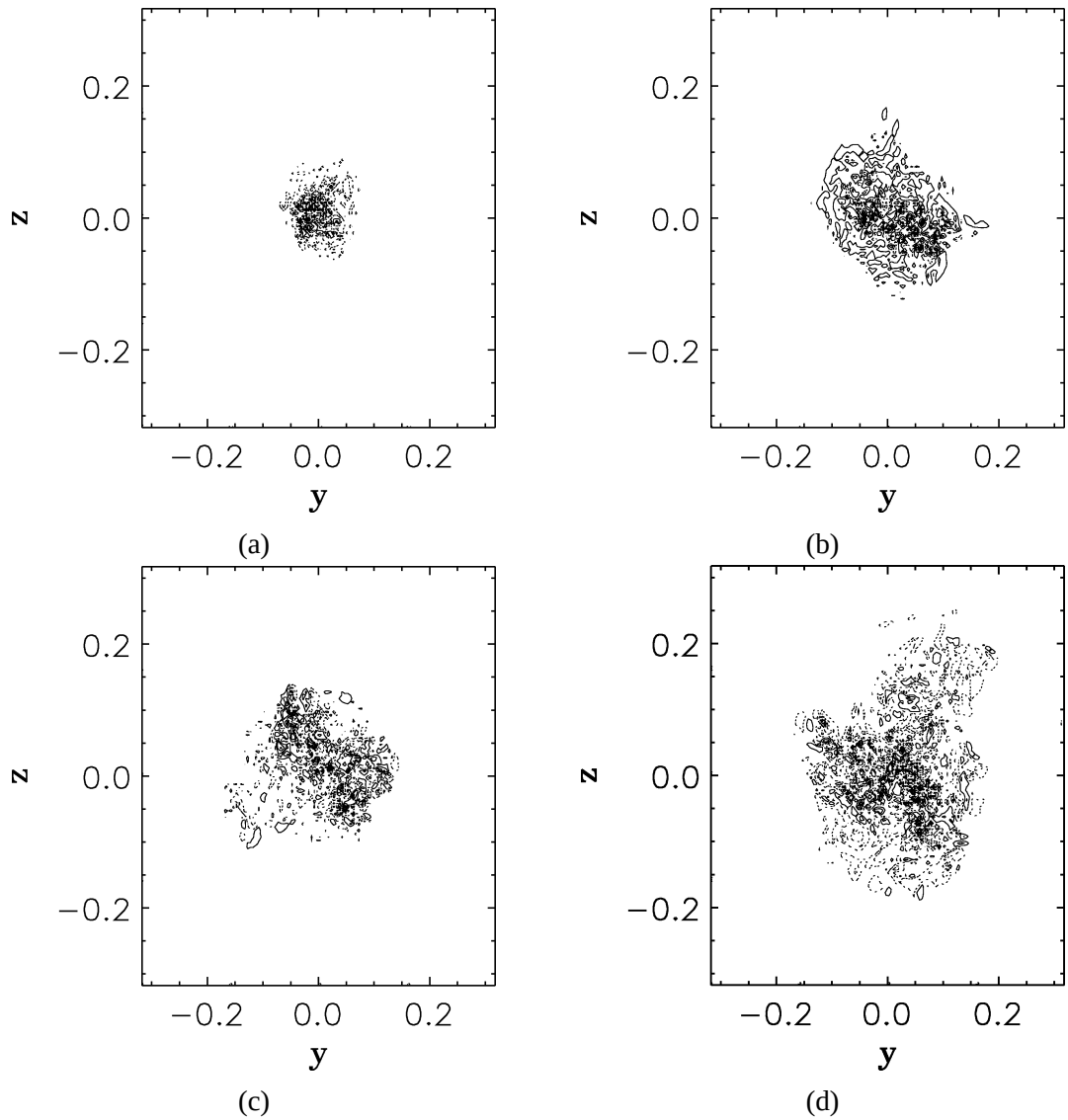

Figure 3. Instantaneous streamwise vorticity contours at YZ plane at $x/D =$: (a) 4; (b) 8; (c) 12; (d) 16 in the plume with azimuthal forcing.

a total vorticity $\omega = \sqrt{\omega_x^2 + \omega_y^2 + \omega_z^2} = 0.6$ and a snapshot of the iso-surface of pressure with a magnitude of $p = 0.024$ is shown in *figure 2(b)*. After a short potential core the large-scale vortices spiral along the plume axis and the small vortices dominate downstream after the breakdown. The spiral and helical mode of plume behaviour can be easily identified in the hydrodynamic pressure field and the spatial evolution can be clearly observed downstream as the plume spreads by entraining mass from the surrounding nonvortical fluid. This is a direct consequence of the entrainment and mixing mechanisms due to the nonlinear interactions of different scales of eddies. More discussions will be given on the issues of entrainment and spreading in the following sections.

Figure 3(a)–(d) displays the snapshots of streamwise vorticity at 2, 6, 10 and 14 diameters across the YZ-plane for the LES with azimuthal forcing, and the corresponding figures for the LES with axisymmetric forcing are shown in *figure 4(a)–(d)*. It can be seen that the flow structure develops slowly from a round

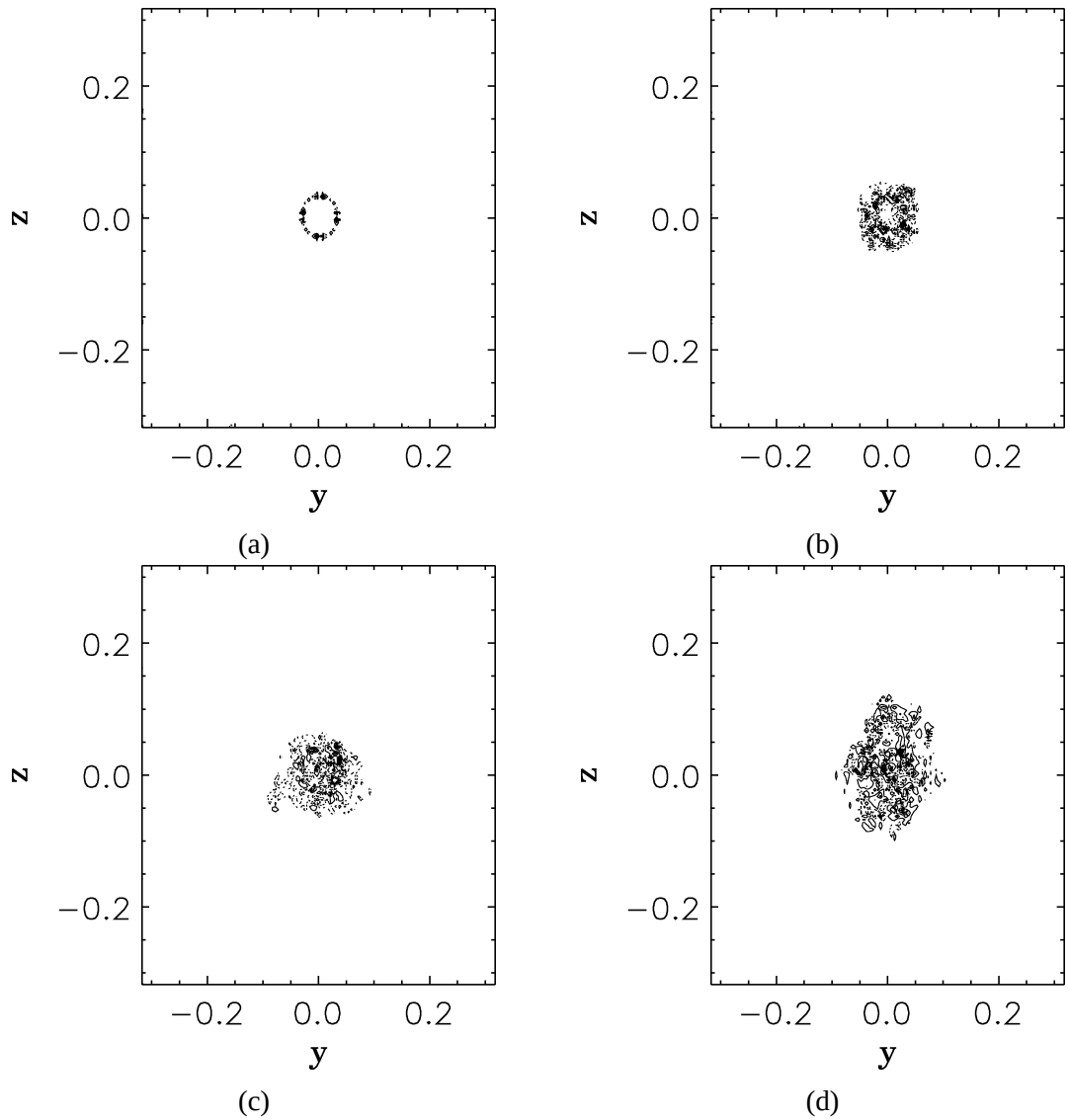

Figure 4. Instantaneous streamwise vorticity contours at YZ plane at $x/D =$: (a) 4; (b) 8; (c) 12; (d) 16 in the plume with axisymmetric forcing.

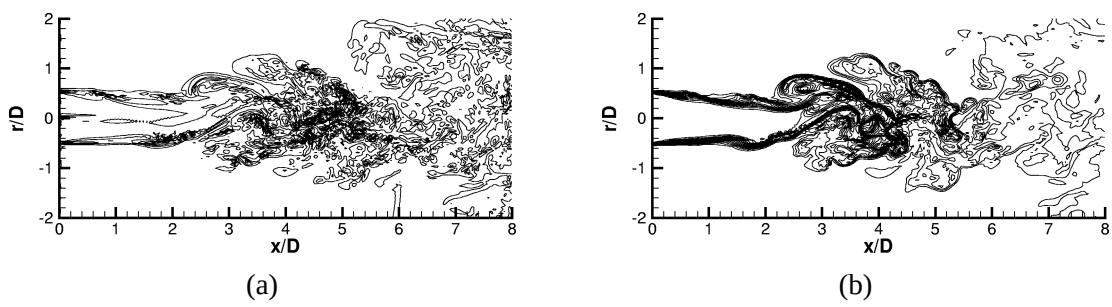

Figure 5. Instantaneous azimuthal vorticity and temperature contours at XY centre-plane of the plume with azimuthal forcing.

ring to an asymmetrical mode for the axisymmetric forcing case. However, with azimuthal forcing, the strong asymmetrical mode of streamwise vorticity grows very rapidly and the plume spreads much earlier than by using axisymmetric mode perturbations. Plotted in *figure 5(a), (b)* are the instantaneous azimuthal vorticity and temperature contours in the centre XY-plane for grid II with azimuthal forcing. These figures depict the vortex sheet rolling-up, vortex stretching and the breakdown to turbulence. The laminar flow continues to dominate the near-field region until the end of potential core, although a helical mode of high lever of perturbations is imposed on the inflow. The flow field looks rather random and loses completely its initial flow characteristics instantaneously further downstream of the plume where it is mainly composed of small eddies. It should be mentioned that some coherent structures which contain many small-scale eddies also exist in the turbulent region. It can also be seen that there exist gaps within the plume which are probably an important mechanism for the entrainment of outer irrotational fluid by the buoyant jet. In the next section it will be shown how a steady state flow field can be obtained by taking samples statistically.

4.2. Statistics

The averaged quantities have been taken over 20 forcing cycles after the initial transients have been swept out of the domain and the flow has reached a statistically steady state.

The LES centerline mean axial velocity distributions with axisymmetric and azimuthal forcings, compared with the experimental measurements of Shabbir and George [12], are plotted in *figure 6(a)*. In the self-similarity plume-like region, the experimental centerline distributions of the mean axial velocity and temperature follow the relationships:

$$U_c = 3.4x^{-1/3}F_0^{1/3}, \qquad T_a/T_c = 1 - 9.4x^{-5/3}F_0^{2/3}/g. \tag{13}$$

It can be seen that the centerline mean velocity and temperature are power functions of height (x) but with different power law. With azimuthal forcing the LES centerline velocity increases rapidly from its initial value to a maximum of around 1.7 times the inflow mean velocity but subsequently decreases rapidly to lower values less than the inflow velocity after about 6 diameters. The initial acceleration of axial velocity is due to the buoyancy acceleration and has also been observed by Lingens et al. [24] who experimentally investigated buoyant jet diffusion flames and by Huang et al. [25] in their experimental work on a plane jet when excited with a varicose mode of instability ($m = 0$). The underlying physical mechanism is that the positive body force $(\rho_a - \rho)g$ constitutes a major part to the mean flow in the near-field region of the present buoyant jet. The rapid decrease of velocity downstream is caused by turbulent mixing with the surrounding fluid. By comparing different initial conditions, one with azimuthal disturbances and the other with axisymmetric disturbances, it can be seen that the helical mode can lead to an earlier and faster decay of centerline velocity with a lower maximum value than the axisymmetric one. Note that a faster decay of centerline velocity implies a larger plume spreading. The LES results with azimuthal forcing are in quite good agreement with experiment and the poorer agreement between the results by the LES with axisymmetric mode and experiment suggests that the azimuthal instability is the dominant mode.

Figure 6(b) shows the centreline distributions of the mean temperature T_c obtained by LES compared to the experimental decay law obeying to $T_a/T_c = 1 - 9.4x^{-5/3}F_0^{2/3}/g$ (George et al. [11]). The mean temperature for the LES results decreases rapidly beyond the end of potential core until the plume-like behaviour is achieved where the decay law is in proportion to $x^{-5/3}$ obtained from experiment. A larger potential core can be observed in the LES results with axisymmetric forcing than those with azimuthal forcing. Again, better agreement with the experimental results can be achieved with azimuthal mode rather than with axisymmetric mode forcing, in the plume-like region. The mean temperature is slightly higher than the ambient temperature (300 K) in the

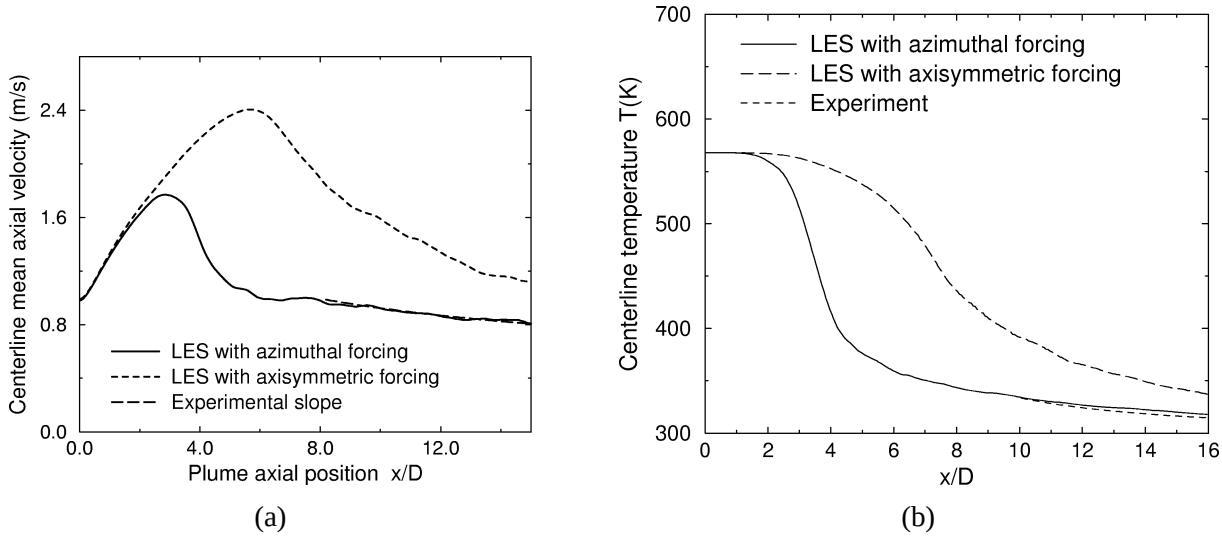

Figure 6. Centerline mean (a) axial velocity, and (b) temperature profiles with azimuthal and axisymmetric forcings.

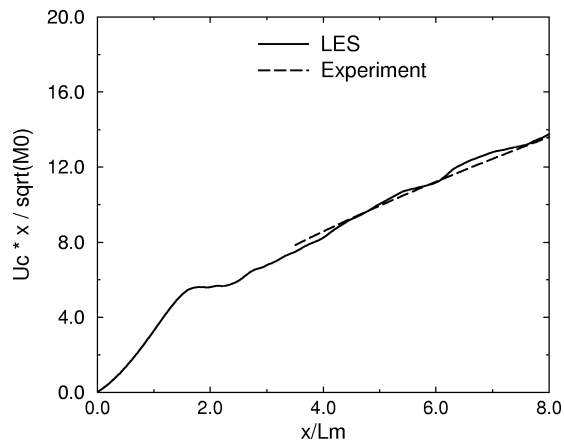

Figure 7. Centerline mean axial velocity profiles by LES and experiment.

plume-like region, especially for the azimuthal forcing, which is caused by strong turbulent mixing with the surrounding air and consequent dilution.

The centerline values of the non-dimensionalized mean velocity $U_c x/\sqrt{M_0}$ as a function of non-dimensional vertical distance $\xi = x/L_M$ are plotted in *figure 7* for the LES results with azimuthal forcing. The experimental distribution of $3.4\xi^{2/3}$ as a function of ξ is shown by the dotted line on the same graph and it can be seen that the agreement between LES and experiment is quite satisfactory. It can be seen that the transition from jet to plume-like behavior occurs at about $\xi = 3$ by the LES.

In a homogeneous environment the buoyant jet eventually becomes plume-like far away from the jet origin even when a large initial momentum flux is added at the source. Gebhart et al. [26] indicated that three regions existed in a forced plume: (1) non-buoyant region near the discharge where the momentum dominates the flow; (2) intermediate region where the influences of the initial momentum forces become weak; and (3) a plume-like region where buoyancy forces dominate the flow. However, the LES results show that there exists another

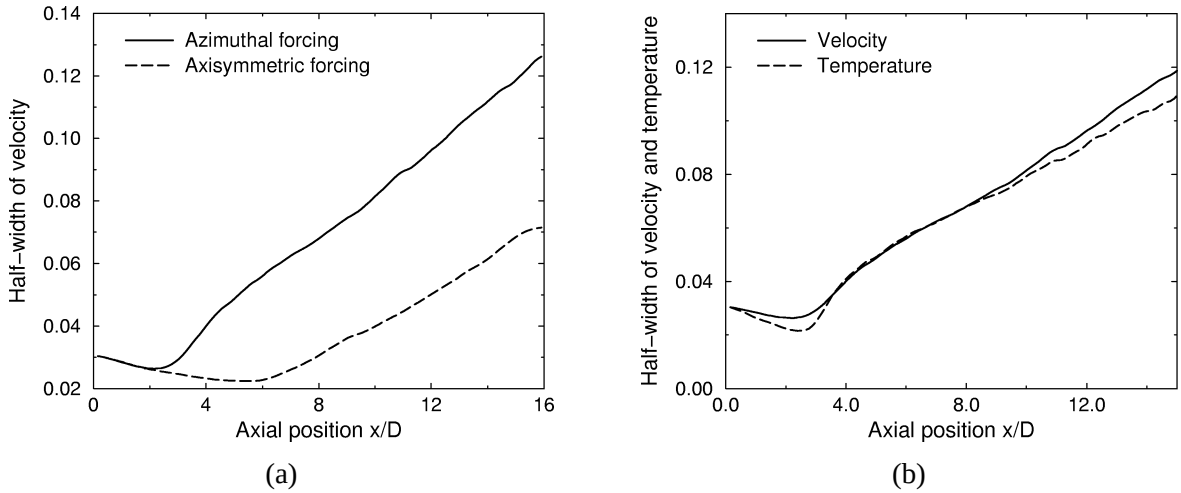

Figure 8. Half-width of: (a) velocity along axial position with axisymmetric and azimuthal forcings; (b) velocity and temperature along axial position.

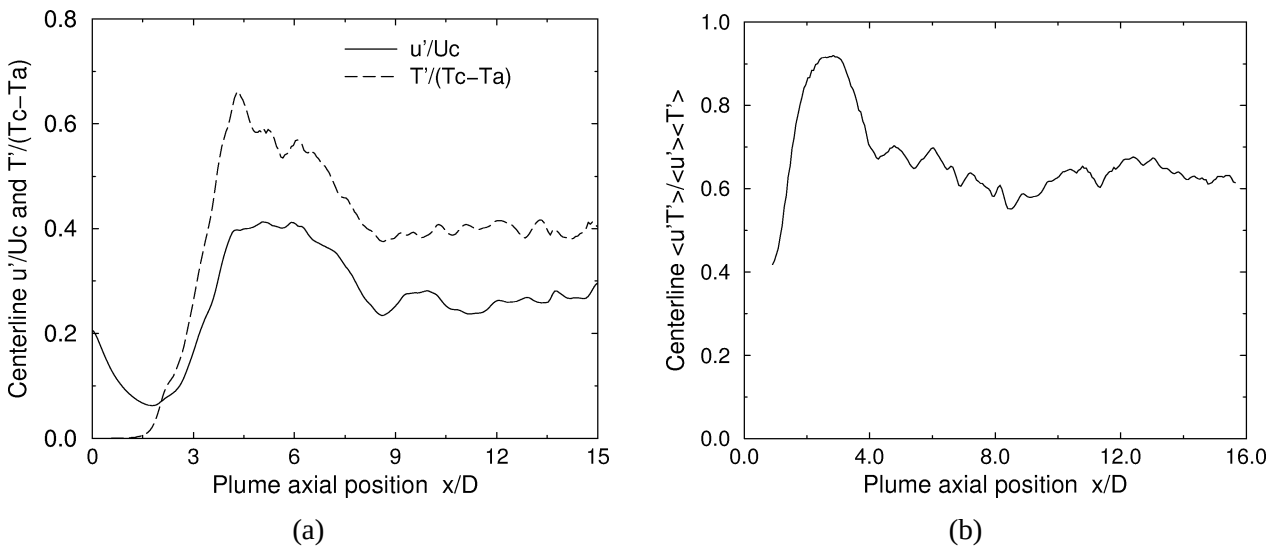

Figure 9. (a) Centerline profiles of turbulence intensity (r.m.s.) of axial velocity and temperature; (b) centerline correlation of fluctuating velocity and temperature.

region from the plume exit to the jet-like region where buoyancy acceleration dominates: a phenomenon has not been mentioned by Gebhart et al. [26].

Figure 8(a) shows LES results of the axial variations of the half-width of velocity (i.e. where the mean axial velocity is half its local centerline value) with axisymmetric and azimuthal forcings. The azimuthal forcing results in a larger spreading rate than the axisymmetric forcing and the plume shows a linear spreading in the zone of established flow. *Figure 8(b)* shows that the half-width of velocity is wider than the half-width for temperature (defined as where the excess mean temperature to the ambient is half the temperature difference between centerline and ambient) in the far-field. This means that the velocity field in a round plume spreads faster than the temperature field and is consistent with the experimental observation of George et al. [11].

The centerline r.m.s. of velocity and temperature normalized by the mean velocity and temperature difference between the local and ambient values ($\Delta T = T - T_a$) are shown in *figure 9(a)*. It should be mentioned that, the implemented outflow boundary condition does affect the higher-order statistics near the outflow boundary, but these are only limited to a small part. Note that at the inflow plane the r.m.s. of velocity is 20% and corresponds to the disturbance level imposed at the inlet. In the potential core region, the r.m.s. velocity and temperature decrease with increasing axial distance which shows a tendency to recover to laminar flow with low turbulence intensities. Beyond the end of the potential core, the fluctuations of velocity and temperature at the centerline increase very rapidly to maximum values but subsequently decrease rapidly to reach nearly constant levels downstream. As can be seen in these figures, the plume goes through a transition accompanied by higher turbulence intensities than the eventual self-similar values downstream of the plume. Crow and Champagne [3] also indicated the same trend in their investigations of isothermal jet under a forcing at a Strouhal number of 0.3. When comparing the centerline profiles of mean velocity and turbulence intensities in *figure 3* and *figure 9(a)*, it can be seen that the first-order mean values reach self-similarity earlier than the second-order turbulent statistics. The velocity-temperature correlation defined by $\overline{u'T'}/(\langle u'\rangle\langle T'\rangle)$ at the centerline is shown in *figure 9(b)*. It is clear that the temperature and velocity fields are strongly coupled in a buoyancy-dominated flow. As can be seen from *figure 9(a)* and *(b)* that the r.m.s. axial velocity, r.m.s. temperature and the velocity-temperature correlation coefficients reach nearly-constant values in the downstream self-similar region and are very close to the experiment of George et al. [11], who reported the following quantities: $(\overline{T'^2})^{1/2}/\overline{\Delta T} = 0.4$, $(\overline{u'^2})^{1/2}/U = 0.28$, $\overline{u'T'}/((\overline{u'^2})^{1/2}(\overline{T'^2})^{1/2}) = 0.6$–$0.7$. The contribution to the heat flux by the turbulence can be examined across the plume by the ratio of $H_T/(H_T + H_M)$, where H_T, H_M are the heat fluxes generated by the mean and turbulence, respectively:

$$H_M = \int_0^\infty UT 2\pi r \,\mathrm{d}r, \qquad H_T = \int_0^\infty \overline{u'T'} 2\pi r \,\mathrm{d}r. \tag{14}$$

In *figure 10* the ratio of $H_T/(H_T + H_M)$ at the axial location of $x/D = 12$ is plotted and it shows that the percentage of the heat flux carried by the turbulence is about 20%.

In order to investigate the influence of grid resolution, we carried out another set of calculations (grid II) at one half of the above (grid I) grid spacing in all three directions. *Figure 11(a)–(b)* shows the comparisons of the centerline mean and r.m.s. axial velocities between grid I and II. It can be seen that the transition from laminar to turbulence occurs a little earlier at the finer grid resolution (II) and that some discrepancies occur close to the exit between these two resolutions. However, both cases show a similar trend and, in general, the statistical

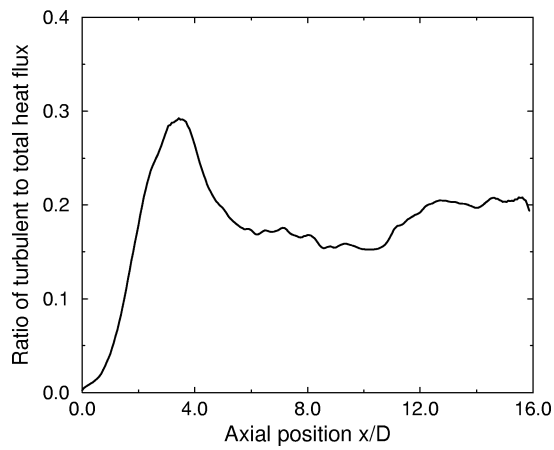

Figure 10. Axial distributions of the ratio of the turbulent heat flux to total heat flux.

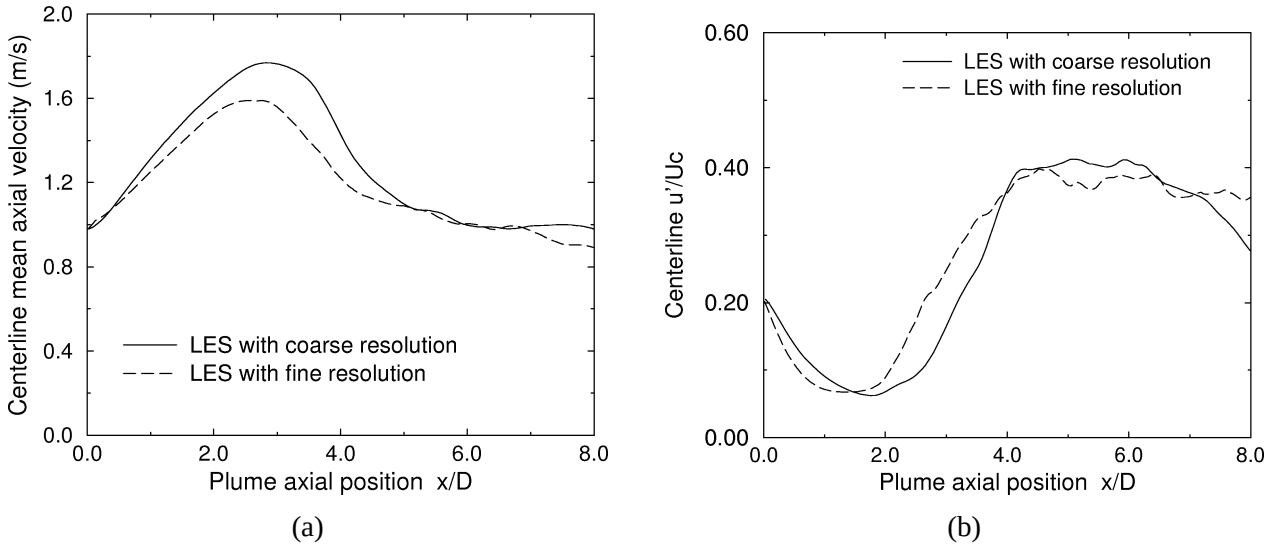

Figure 11. Comparisons of the centerline (a) mean and (b) r.m.s. axial velocity between coarse and fine resolutions.

quantities are in reasonable agreement with each other beyond the end of potential core except close to the end of the domain for grid II which is probably slightly affected by the outflow boundary condition. Therefore, it is sufficient to use grid I to obtain the statistical results in the self-similar region. On the other hand, to capture the plume-like behaviour in the far-field rather than the near-field plume dynamics is of our major interest in the present forced buoyant jet.

4.3. Self-similarity

The tendency for a plume to become self-similar some distance downstream of a plume means that the turbulent flow depends only on the initial momentum flux and initial weight deficit and that the overall properties at all vertical heights above the plume base obey the same rules (e.g. Gaussian profile) over a wide range of scales. The relationship of the dependent and independent variables can be obtained by dimensional analysis, see, for instance, Tennekes and Lumley [10] who deduced similarity solutions of axisymmetric plumes. There exist unknown empirical constants in the self-similar Gaussian profiles which need to be confirmed by experiments and George et al. [11] obtained such self-preserving profiles as follows:

$$\frac{U}{U_c} = \exp\left(-55r^2/x^2\right), \qquad \frac{T - T_a}{T_c - T_a} = \exp\left(-65r^2/x^2\right). \tag{15}$$

These imply a slightly greater spread of momentum relative to buoyancy.

If self-similarity is achieved in a plume, same shapes should be maintained at different downstream locations for the radial profiles of mean velocity, temperature and their fluctuations. The four axial positions ($x/D =$ 8, 10, 12, 14) are chosen to examine the radial profiles across the plume. The radial profiles of velocity and temperature from LES results and the experiments of George et al. [11] are shown in *figure 12(a)* and *(b)*, where x_0 is the origin of jet. Note that $x_0 = 0.5D, 1.1D$ is different for the azimuthal and axisymmetric forcings and is calculated as the slope of a plot of $U^3\,x$ versus U^3 as suggested in the appendix A of George et al. [11]. The normalized r.m.s. of axial, radial and tangential velocity profiles are plotted in *figure 13*. It is shown that the turbulence intensities for the radial and tangential velocity are smaller than that of axial velocity. The peak is off-axis in the profile of axial velocity fluctuations and it should be noted that there is some asymmetry near

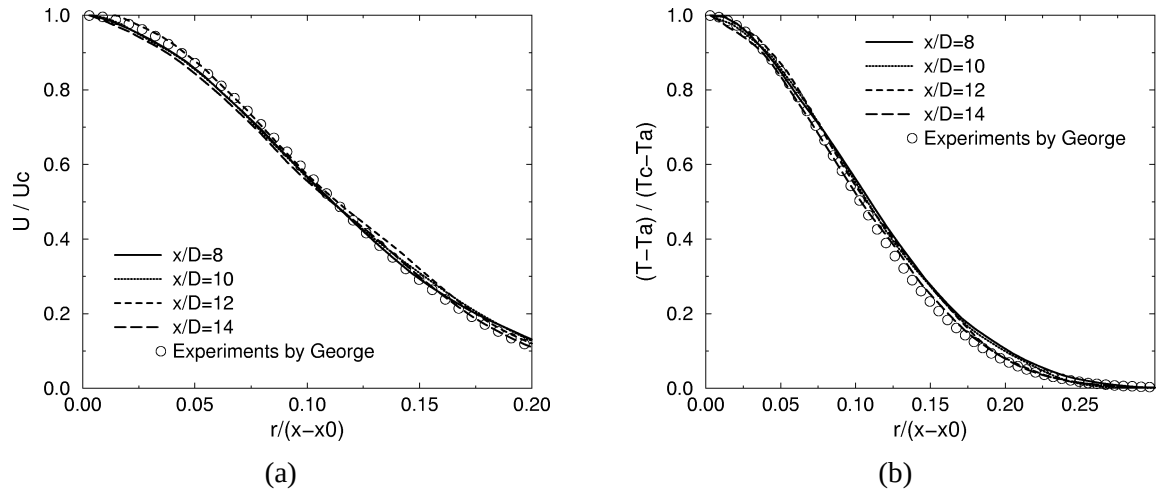

Figure 12. Radial profiles of (a) mean axial velocity, and (b) mean temperature at four axial positions compared with experiment.

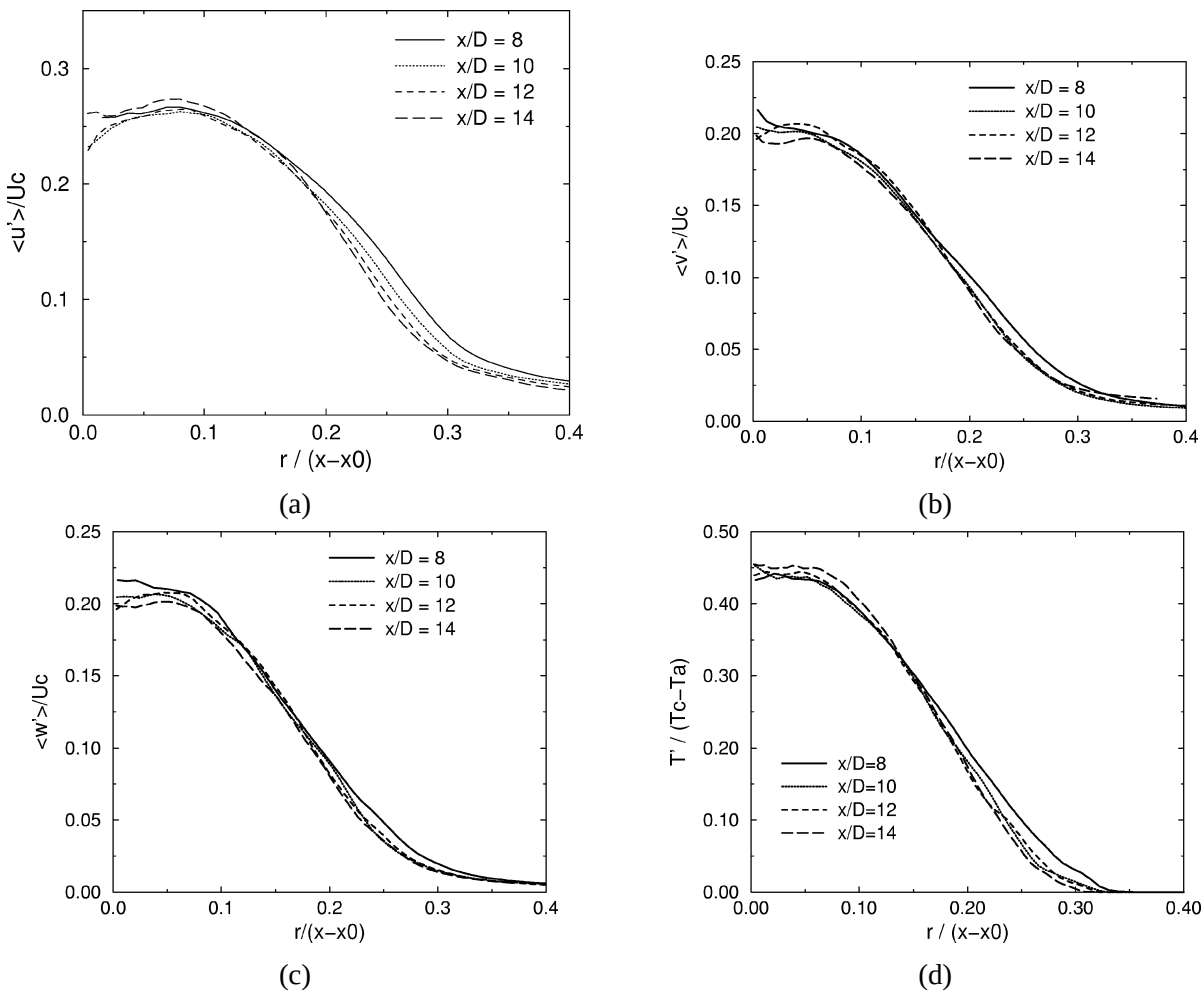

Figure 13. Radial profiles of: (a) axial velocity fluctuations; (b) radial velocity fluctuations; (c) tangential velocity fluctuations, and (d) temperature fluctuations at four axial positions.

the plume axis and is caused by insufficient sampling. The radial profiles of turbulent temperature fluctuations are plotted in *figure 13(d)* where it can be seen that the centerline value of temperature (or the scalar) intensity is about 0.45. This is substantially higher than the 0.20–0.25 for jets and is due to buoyancy intensifying the turbulence field. This agrees well with the result reported by Papanicolaou and List [20] and Dai [17], but it is a little higher than the 0.40 reported by George et al. [11]. The self-similarity of the higher-order statistics has not yet been achieved at 8 diameters and is consistent with the centerline distributions shown in *figure 9(a)*. Self-similar behaviour can only be achieved at larger distances for turbulence than for mean quantities such as velocity and temperature.

The radial profiles of the shear stress and vertical turbulent heat flux at the same four positions as mentioned above are shown in *figure 14*. These second moments are plotted in terms of the similarity variables. The shear stress profile $\overline{u'v'}F_0^{-2/3}x^{2/3}$ has a maximum value close to the value of 0.32 reported by [12] at around $r/(x-x_0) = 0.08$. Its shape resembles the mean velocity gradient so that the maximum shear stress is located in

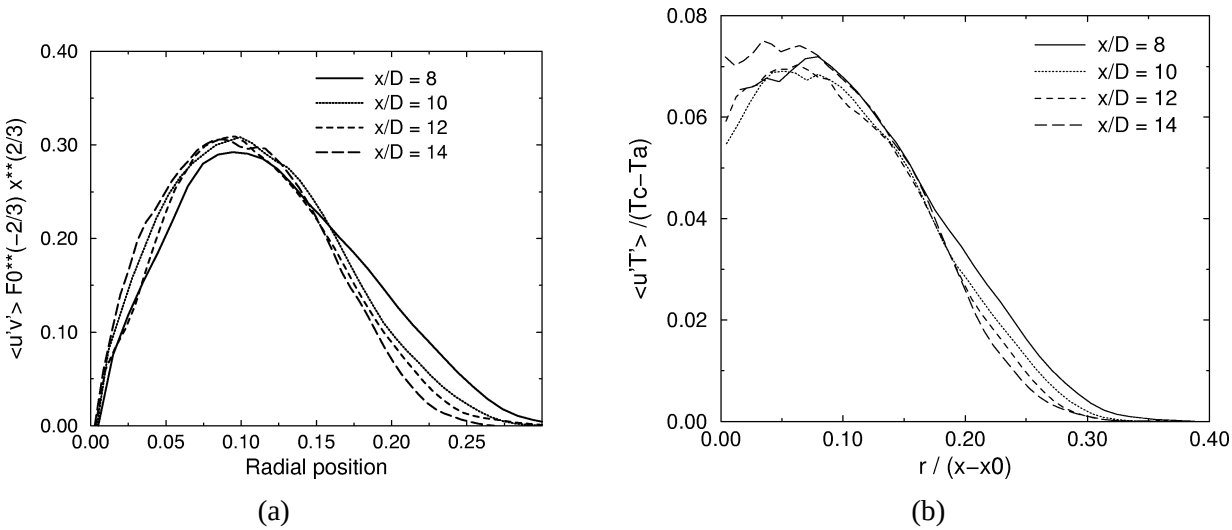

Figure 14. Radial profile of the: (a) turbulent shear stress, and (b) vertical turbulent heat flux, at four axial positions.

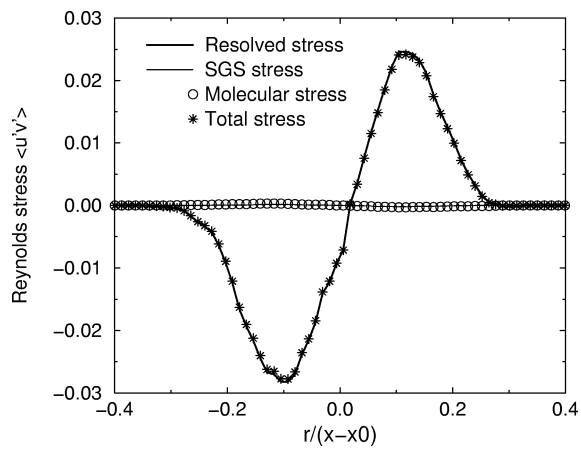

Figure 15. Resolved, SGS and molecular shear stresses contributed to the total shear stress along radial direction.

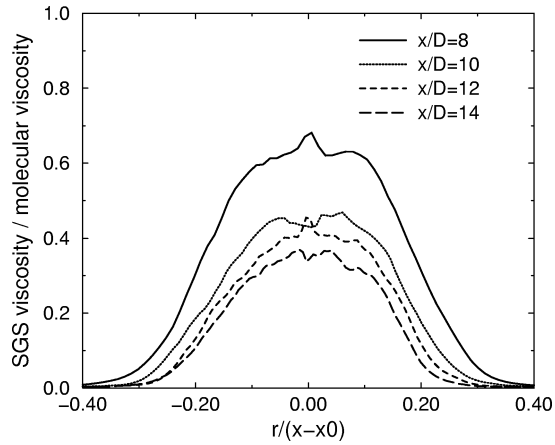

Figure 16. Radial profiles of the ratio of SGS viscosity to molecular viscosity.

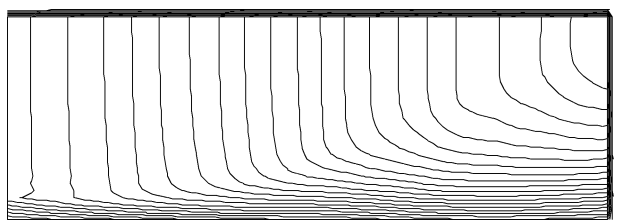

Figure 17. The streamlines of mean velocity field in the plume.

the shear layer between the plume and surrounding air. No shear stress exists on the plume axis and an off-axis peak is also observed in the correlation coefficient profile. The profile of the transport term $\overline{u'T'}$ follows the shape of turbulence intensity of either velocity, or temperature.

In order to investigate the role of the Smagorinsky SGS model, it is necessary to examine the Reynolds stresses $\langle u'v'\rangle$. *Figure 15* shows the radial profiles of resolved stress $\overline{uv}$, SGS stress $-\overline{\nu_t}\,(\frac{\partial U}{\partial r}+\frac{\partial V}{\partial x})$, molecular stress $-\nu\,(\frac{\partial U}{\partial r}+\frac{\partial V}{\partial x})$ and the total stress at the axial location of $x/D=12$. It can be seen that the subgrid-scale stress contributes little to the total shear stress so that the flow field is nearly fully resolved with the present grid resolution and the lower Reynolds number in the present LES may cause such a relatively small influence of SGS. The ratio of the average SGS eddy viscosity $\overline{\nu_t}$ to the molecular viscosity ν is plotted in *figure 16*. It is clear that the SGS viscosity is even smaller than the molecular viscosity with the maximum value found near the centerline. The self-preserving eddy viscosity far from the inlet is smaller than that in the intermediate region.

4.4. Entrainment

The streamlines of the mean velocity fields are plotted in *figure 17* and show very similar results to that according to the boundary layer theory by Schlichting [27] and the DNS by Boersma et al. [13]. It can be seen that the plume draws in ambient fluid through the lateral boundary. This is a result of the so-called 'entrainment'. Cortesi et al. [28] explained that the entrainment was a direct consequence of the engulfment of fluid by the coherent, vortical structures after the roll-up and pairing (amalgamations) of the vortex. The

entrainment or mixing of surrounding fluid into the plume engulfed by the turbulent eddies is key to the understanding of turbulent plumes.

Normally, the ambient temperature gradient is assumed to be negligible and such an assumption can simplify plume theory considerably – we will investigate this further. The basic assumption of plume theory based on the Boussinesq approximation is that the mean entrained flux across the edge of the plume E (entrainment rate) is proportional to the local upward velocity W (a function of plume height). The description of the plume is simplified by taking the cross-sectional average of the mass flux, momentum flux and buoyancy flux as functions of vertical height to obtain the top-hat variables such as plume radius, vertical velocity and reduced gravity. Of practical interest is the determination of the entrainment rate on the basis of the assumption introduced by Morton et al. [29]. An entrainment coefficient is defined as:

$$\alpha = \frac{E}{bW}, \tag{16}$$

where E, W, b are known as the top-hat variables of entrainment rate, local vertical velocity and plume width and are defined as (Turner [1]):

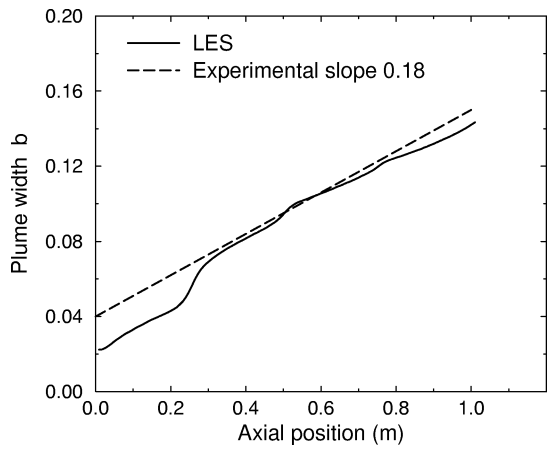

Figure 18. Plume width distribution along axial position.

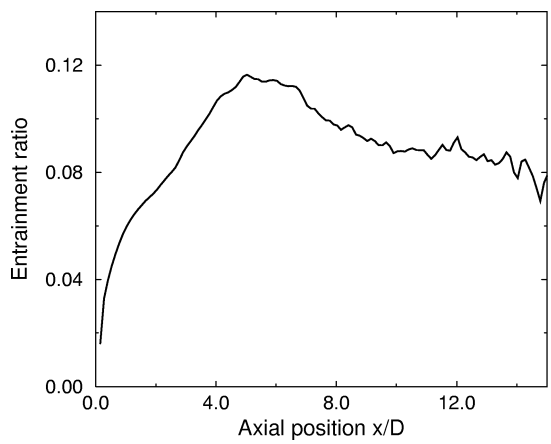

Figure 19. Plume entrainment ratio along axial position.

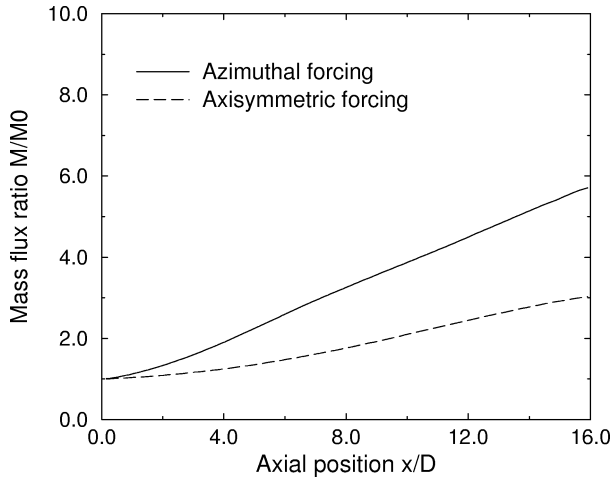

Figure 20. Mass flux ratio distribution along axial position.

$$
\begin{aligned}
b^2 W &= \int_0^\infty U r \,\mathrm{d}r, \\
b^2 W^2 &= \int_0^\infty U^2 r \,\mathrm{d}r, \\
E &= \frac{\mathrm{d}}{\mathrm{d}x}\left(\int_0^\infty U r \,\mathrm{d}r\right).
\end{aligned}
\tag{17}
$$

The calculated plume width b by the LES with azimuthal forcing, defined by the above equation, is shown in *figure 18*. The experimental slope of 0.18 is also plotted in the same graph and, it can be seen, that the agreement is good. *Figure 19* shows that the entrainment ratio initially increases rapidly to reach its peak value of about 0.12 at around four diameters and subsequently decreases to a relatively steady value of 0.09. This compares well with the experimental value of $0.153/\sqrt{2} = 0.108$. Here $\sqrt{2}$ is used because Shabbir and George [12] used a different definition (number 2 is included in the entrainment E) from others (Turner [1]).

Entrainment enhancement can also be shown by considering the mass flux ratio (defined as the ratio of the mass flux at a fixed axial location over the inflow mass flux). The mass flux across the plume is given by:

$$
M = \int_0^\infty \rho U 2\pi r \,\mathrm{d}r. \tag{18}
$$

Figure 20 depicts the distribution of the mass flux ratio along the axial position. In the near field region the mass flux is increasing slowly because it lies in the laminar potential region whilst, after around 4 diameters, the mass flux then increases rapidly due to the strong turbulent mixing and entrainment. *Figure 20* also shows that the thermal plume grows linearly and the azimuthal forcing leads to a larger entrainment than the axisymmetric mode.

4.5. Budget analysis

By plotting terms in the energy budget, it can clearly be seen how each term varies in relation to others and is useful in identifying dominant physical processes. The resolved governing equations for the mean axial velocity and energy (in terms of temperature difference, $\Delta T = T - T_a$) in cylindrical coordinates for the axisymmetric case (after neglecting viscous diffusion) are as follows:

$$\underbrace{\frac{\partial(\rho U^2)}{\partial x}}_{\text{Vertical convection}} + \underbrace{\frac{1}{r}\frac{\partial(r\rho UV)}{\partial r}}_{\text{Radial convection}} \approx \underbrace{-\frac{\partial p}{\partial x}}_{\text{Pressure gradient}} + \underbrace{(\rho_a - \rho)\,g}_{\text{Buoyancy}} - \underbrace{\frac{\partial(\rho\overline{u'^2})}{\partial x}}_{\text{Vertical transport}} - \underbrace{\frac{1}{r}\frac{\partial(r\rho\overline{u'v'})}{\partial r}}_{\text{Radial transport}},$$

$$\underbrace{\frac{\partial(\rho U\Delta T)}{\partial x}}_{\text{Vertical convection}} + \underbrace{\frac{1}{r}\frac{\partial(r\rho V\Delta T)}{\partial r}}_{\text{Radial convection}} \approx - \underbrace{\frac{\partial(\rho\overline{u'T'})}{\partial x}}_{\text{Vertical transport}} - \underbrace{\frac{1}{r}\frac{\partial(r\rho\overline{v'T'})}{\partial r}}_{\text{Radial transport}}. \tag{19}$$

The radial profile of the balance of axial mean momentum at the axial location of $x/D = 12$ in the self-similar plume-like region, is shown in *figure 21(a)*, where it can be seen that the vertical convection, buoyancy force and radial turbulent transport are the dominating terms in the budget. The vertical turbulent transport is negligible compared to the radial one because turbulent mixing mainly occurs in the radial direction through entrainment by the vortex mechanism. It can also be seen that the radial convection term is smaller than the vertical convection and that the radial turbulent transport nearly balances the streamwise convection and the buoyancy force in the axial momentum equation. The pressure gradient along the streamwise direction is also negligible and is much smaller than the radial pressure gradient (which is not shown here).

The radial distributions of the balance of mean energy at $x/D = 12$ are plotted in *figure 21(b)*. It can be seen that the radial convection term is rather small compared to the vertical convection term and is due to the fact that the streamwise velocity dominates the flow field and convects energy downstream. The vertical convection term nearly balances the radial transport in the energy equation and the buoyancy implicitly influences the heat transfer through the vertical convective term. The maximum magnitude of the radial transport term is about 50 and is very close to the experimental value reported by Shabbir and George [12].

Comparing the above two figures, one can see that the radial turbulent transport is one of the dominating terms in both mean momentum and energy equations and is due to turbulent mixing of small eddies by large scale eddies occurring mainly along the radial direction. It can also be seen that the radial convection is not so important as the vertical convection and that the convective and turbulent transport terms in the momentum equation have the same trend as the corresponding ones in the energy equation. It will also be noticed that, because of numerical, statistical and/or modeling errors the imbalances in these budgets do not fall to zero. However, these errors are much smaller than the dominant terms in the budgets.

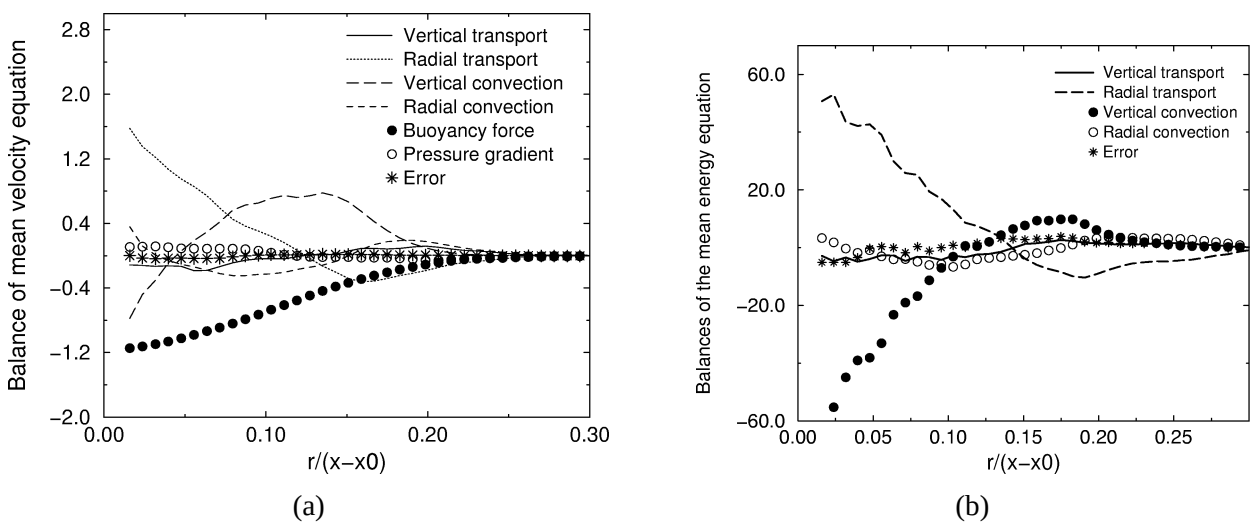

Figure 21. Balances of the: (a) mean momentum and (b) energy equations.

5. Summary and conclusions

A forced plume has been simulated using LES at a Reynolds number of 1273 and a density ratio of about 2.0. The numerical implementation is based on a projection method for low-Mach number weakly compressible flows and the simulations reproduce the typical spatial development of a turbulent buoyant jet. Several conclusions have been drawn from the present LES:

(1) As with cold jets, plumes can also have several stages of vortex development such as roll-up and breakdown. The spreading of the plume is strongly affected by instability modes and the helical mode can lead to larger spreading and entrainment than the axisymmetric mode. From the instantaneous vorticity field, one can observe strong turbulent mixing across the centerline by the helical mode of instability. The statistical results show that the centerline fluctuating velocity components and fluctuating temperature are not small and are caused by three-dimensional rotational vortex dynamics. The energy-spectrum for the axial velocity fluctuations shows the $-5/3$ power law of the Kolmogorov decay, whilst the power spectrum for temperature shows both $-5/3$ and -3 power laws in the inertial-convective and inertial-diffusive ranges.

(2) Rather differently to non-buoyant jets, the centerline mean velocity increases in the near-plume-exit region due to the buoyancy acceleration and subsequently decays by the strong turbulent transport in the forced plume. The centerline profile of mean velocity (normalized by $xM_0^{1/2}/F_0$) demonstrates the transition from momentum- to buoyancy-dominated flow and the slope within the asymptotic plume-like structure compares well with the experimental slope of $2/3$. The present LES can accurately capture the changing behaviour from jet to plume-like in addition to the above mentioned transition from laminar to turbulence.

(3) When comparing different type of forcing at the inlet, it can be found that the LES results by the azimuthal forcing are in much better agreement with experiment than those with axisymmetric forcing in terms of the centerline mean velocity distribution, plume spreading, etc. Self-similarity can be achieved some diameters downstream with respect to the radial profiles of mean velocity and temperature. However, similarity for higher-order statistics is less apparent than for the first-order mean statistics. The self-similar quantities of the fluctuations of velocity and temperature and their correlation at the centerline agree well with the corresponding experimental ones. The strong interactions of turbulence and buoyancy lead to higher r.m.s. of scalar fluctuations.

(4) The comparisons between the present LES results with azimuthal forcing and the plume theory are considered to be good. We obtained the distributions of entrainment ratio and the plume width along the vertical direction according to plume theory. The entrainment ratio is around 0.09 and the plume width is nearly proportional to the plume height with a slope of about 0.18 and is consistent with experimental values.

(5) In the mean momentum and energy budgets, it is found that the radial turbulent transport is much larger than axial transport and that the vertical convection is much larger than radial convection. In the axial momentum equation the radial turbulent transport nearly balances the sum of the streamwise convection and buoyancy force. Whilst, in the energy equation, the radial turbulent stress is nearly balanced by the streamwise convection.

Acknowledgment

The work is supported by the Fire Research Station (FRS) and EPSRC under the grant GR/L58699. Useful discussions with Professor George of the Sate University of New York at Buffalo are greatly appreciated. The calculations are conducted on the T3E parallel computer at Manchester University.

References

[1] Turner J.S., Buoyant plumes and thermals, Annu. Rev. Fluid Mech. 1 (1969) 29–44.
[2] Urbin G., Metais O., Large-eddy simulation of three-dimensional spatially-developing jets, in: Voke P.R., Kleiser L., Chollet J.P. (Eds.), Direct and Large-Eddy Simulation, the First ERCOFTAC Workshop on Direct and Large-Eddy Simulation, 1997, pp. 35–46.
[3] Crow S.C., Champagne F.H., Orderly structure in jet turbulence, J. Fluid Mech. 48 (1971) 547–591.
[4] Yuan L.L., Street R.L., Ferziger J.H., Large-eddy simulations of a round jet in crossflow, J. Fluid Mech. 379 (1999) 71–104.
[5] Nam S., Bill R.G., Numerical simulation of thermal plumes, Fire Safety J. 21 (1993) 231–256.
[6] Michalke A., Survey on jet instability theory, Prog. Aerospace Sci. 21 (1984) 159–199.
[7] Luo K.H., Sandham N.D., Instability of vortical and acoustic modes in supersonic round jets, Phys. Fluids 9 (1997) 1003–1013.
[8] Grinstein F.F., DeVore C.R., Dynamics of coherent structures and transition to turbulence in free square jets, Phys. Fluids 8 (1996) 1237–1251.
[9] Zaman K.B.M.Q., Spreading characteristics of compressible jets from nozzles of various geometries, J. Fluid Mech. 383 (1999) 197–228.
[10] Tennekes H., Lumley J.L., A First Course in Turbulence, MIT Press, Cambridge, 1972.
[11] George W.K., Alpert R.L., Tamanini F., Turbulence measurements in an axisymmetric buoyant plume, Int. J. Heat Mass Tran. 20 (1977) 1145–1154.
[12] Shabbir A., George W.K., Experiments on a round turbulent buoyant plume, J. Fluid Mech. 275 (1994) 1–32.
[13] Boersma G.J., Brethouwer G., Nieuwstadt F.T.M., A numerical investigation on the effect of the inflow conditions on the self-similar region of a round jet, Phys. Fluids 10 (1998) 899–909.
[14] Menon A., Rizk M., Large-eddy simulations of forced three-dimensional impinging jets, Int. J. Comput. Fluid Dyn. 7 (1996) 275–289.
[15] Rooney G.G., Linden P.F., Similarity considerations for non-Boussinesq plumes in an unstratified environment, J. Fluid Mech. 318 (1996) 237–250.
[16] Woods A.W., A note on non-Boussinesq plumes in an incompressible stratified environment, J. Fluid Mech. 345 (1997) 347–356.
[17] Dai Z., Tseng L.K., Faeth G.M., Structure of round, fully developed, buoyant turbulent plumes, J. Heat Trans-T ASME 116 (1994) 409–417.
[18] List E.J., Turbulent jets and plumes, Annu. Rev. Fluid Mech. 14 (1982) 189–212.
[19] Noto K., Teramoto K., Nakajima T., Spectra and critical Grashof numbers for turbulent transition in a thermal plume, J. Thermophys. Heat Tr. 13 (1999) 82–90.
[20] Papanicolaou P.N., List E.J., Investigations of round vertical turbulent buoyant jets, J. Fluid Mech. 195 (1988) 341–391.
[21] Najm H.N., Wyckoff P.S., Knio O.M., A semi-implicit numerical scheme for reacting flow, J. Comput. Phys. 143 (1998) 381–402.
[22] Olsson M., Fuchs L., Large eddy simulation of a forced semiconfined circular impinging jet, Phys. Fluids 10 (2) (1998) 476–486.
[23] Kotsovinos N.E., Turbulence spectra in free convection flow, Phys. Fluids A 3 (1) (1991) 163–167.
[24] Lingens A., Reeker M., Schriber M., Instability of buoyant diffusion flames, Exp. Fluids 20 (1996) 241–248.
[25] Huang J.M., Hsiao F.B., On the mode development in the developing region of a plane jet, Phys. Fluids 11 (1999) 1847–1857.
[26] Gebhart B., Jaluria Y., Mahajan R.L., Sammakia B., Buoyancy-Induced Flows and Transport, Hemisphere, New York, 1988.
[27] Schlichting H., Boundary-layer Theory, 7th ed., McGraw-Hill, New York, 1979.
[28] Cortesi A.B., Smith B.L., Yadigaroglu G., Banerjee S., Numerical investigation of the entrainment and mixing processes in neutral and stably-stratified mixing layers, Phys. Fluids 11 (1) (1999) 163–185.
[29] Morton B.M., Taylor G.I., Turner J.S., Turbulent gravitational convection from maintained and instantaneous sources, P. Roy. Soc. Lond. A 234 (1958) 1–23.